The effect of slip on the development of flow separation due to a bump in a channel

Silvia Ceccacci¹, Sophie A.W. Calabretto², Christian Thomas¹,† and James P. Denier³

(Received 23 January 2022; revised 7 August 2022; accepted 9 October 2022)

A numerical study on the effect of surface slip on the flow in a constricted channel is presented, with the aim of exploring the use of surface slip to control flow separation. Our focus is on two-dimensional flow in a channel over a bump, with a fixed aspect ratio, upon which a Robin-type slip boundary condition is imposed. When the channel walls are fully no-slip, such a flow is known to develop a region of separation behind the bump, at sufficiently large Reynolds numbers. The effect of slip on the separation bubble dynamics occurring behind the bump is investigated, for Reynolds numbers 2000 and 4000. It is shown that surface slip (i) attenuates the intensity of separation as it diminishes the minimum of the streamwise velocity within the recirculation region; (ii) delays the onset of flow separation, shifting it downstream, along the bump, and (iii) reduces the dimensions of the separation bubble behind the bump, allowing the flow to reattach sooner. Ultimately, slip inhibits separation, with both the points of separation and reattachment coalescing, for a slip length λ of approximately 0.2.

Key words: channel flow, separated flows, computational methods

1. Introduction

Flow separation is the detachment of a viscous fluid layer from a body surface. It results in flow reversing its direction and is effectively driven by an adverse pressure gradient, which may arise due to significant regions of surface curvature such as corners on a body's surface (in the case of external flows) or geometry constrictions (in the case of internal flows); an excellent description of flow separation can be found in Sychev *et al.*

† Email address for correspondence: christian.thomas@mq.edu.au

© The Author(s), 2022. Published by Cambridge University Press. This is an Open Access article, distributed under the terms of the Creative Commons Attribution licence (http://creativecommons.org/licenses/by/4.0), which permits unrestricted re-use, distribution and reproduction, provided the original article is properly cited.

¹School of Mathematical and Physical Sciences, Macquarie University, NSW 2109, Australia

²School of Engineering, University of Leicester, Leicester LE1 7RH, UK

³Reined in Solutions, Sydney, NSW 2075, Australia

(1998). Amongst other potential negative impacts, flow separation can directly lead the flow to transition from a laminar to a turbulent state, which in most cases is considered detrimental (Hanks 1963). In aerodynamics, flow separation significantly impacts lift, and laminar–turbulent transition contributes to an increase in the friction component of drag. In particular, skin-friction drag is one of the largest contributors to aerodynamic drag in commercial aircraft. The implications of such increases thus impact globally on both an economical and environmental level. Although fuel efficiency is one of the main concerns in the aircraft industry, requirements on environmentally friendly transports are providing an added impetus for more fuel-efficient aircraft.

Studies of laminar–turbulent transition, with the aim to delay transition or, ideally, avoid transition, continue to be a focus of international research efforts. On one hand, focus is drawn to receptivity mechanisms and how they trigger internal instabilities (Sengupta *et al.* 2018). Such instabilities develop in space and time, potentially leading to laminar–turbulent transition. On the other hand, external disturbances are also of interest as they may influence the flow through different growth mechanisms. In fact, an approaching unstable Tollmien–Schlichting wave to a surface can have a significant impact on transition, especially if the surface has localised imperfections (Xu *et al.* 2016; Xu, Lombard & Sherwin 2017). Because of its potential to trigger early transition, the ability to control flow separation is considered crucial in many technological applications. One way of achieving this is through an alteration of the pressure gradient, which can be obtained by modifying the shape of the surface over which the fluid flows. For this reason, significant effort has gone into the design of aerodynamic and hydrodynamic surfaces that delay flow separation and ensures the local flow remains attached for as long as possible.

As flow separation occurs on the surface of the body, it becomes natural to explore different ways in which the surface itself could be modified to control it. One approach is to slightly alter the shape of the surface, introducing a particular texturing, such as dimples or spherical beads (Beratlis, Balaras & Squires 2018). Alternatively, the surface can be made slippery (or non-wettable) using the developments in surface chemistry and laser physics (Vorobyev & Guo 2015). These types of surfaces, known as superhydrophobic, have been shown to be effective in reducing turbulent frictional drag in water (Wang & Gharib 2020) and when the stability of the Cassie–Baxter state is achieved (Chang & Lu 2020).

According to the Navier slip model (Navier 1823), a slip wall is typically quantified by a slip length λ , which is the artificial distance below the slipping surface where the velocity goes to zero. In other words, in the modelling of fluid flow over a slippery surface, it is assumed that the fluid immediately adjacent to the surface has non-zero tangential velocity. This corresponds to a Knudsen number $K_n = \gamma/L$ between 10^{-3} and 10^{-1} , where γ is the mean free path of the fluid molecules and L is a characteristic length scale. For moderate levels of wall slip, experimental results have shown excellent agreement with the linearised Navier slip model (Thompson & Troian 1997). Results by Wang & Hadjiconstantinou (2019) and Hadjiconstantinou (2021), based upon first-principles atomistic models, confirm the utility of the linearised Navier model. We will adopt a linear Navier-slip approach throughout this work. In this case, the flow can be classified as being in a, so-called, slip-flow regime where the system dynamics can be modelled with the Navier-Stokes equations combined with slip boundary conditions. It was shown by Matthews & Hill (2008) that as the slip length λ increases, the rate of change of the tangential velocity decreases. This happens because the velocity on the solid surface is no longer zero and slips with a velocity that increases with the slip length.

There have been many studies on the impact of slip on both suppression of instabilities and a reduction in turbulent drag production; see for example Lauga & Cossu (2005) and

Min & Kim (2004), and references contained therein. Lauga & Cossu (2005) undertook a linear stability analysis of the flow in a channel with slip applied to both lower and upper walls. Slip was found to increase the critical Reynolds number for linear instability, especially when slip is applied on both walls. Min & Kim (2004) also found that the direction of slip plays an important role in channel flow dynamics. Exploiting direct numerical simulations (DNS) of turbulent channel flow, they demonstrated that slip applied in the streamwise direction led to a decrease in turbulent skin friction, whereas slip applied in the spanwise direction was found to increase turbulent drag.

In this paper, we consider the two-dimensional channel flow with a Gaussian-shaped bump. Introducing a curvilinear obstacle between the two flat plates establishes flow separation behind the obstacle, which increases in magnitude as the Reynolds number increases (Smith 1976; White & Smith 2012). However, it has been shown, for the flow past a circular cylinder, that a generic slip boundary condition has a significant effect in controlling flow separation and decreasing its intensity (Legendre, Lauga & Magnaudet 2009). The aim of the current work is to combine these two approaches, by introducing a moderate curvature in the geometry and applying slip along its length. Thus, the influence of a slip boundary condition on the flow over a bump is investigated, with particular attention to the question, can slip inhibit flow separation in such cases? In § 2, we formulate the problem and provide the salient details of the numerical methods used in our DNS; in § 3, we present our results on the influence of slip on the channel flow dynamics, describing the features that highlight its effectiveness in reducing laminar flow separation. Finally, in § 4, conclusions are drawn with a discussion on possible future extensions.

2. Formulation

2.1. The model

Consider a two-dimensional incompressible fluid with kinematic viscosity v^* , flowing in a channel of half-width h^* . The direction normal to the channel walls is denoted by y^* , and x^* measures the distance along the channel. (Here an asterisk denotes dimensional quantities.) The channel has a Gaussian-shaped bump located along the lower wall. If the channel surfaces are taken to be both impermeable and no-slip then, under suitable conditions on the bump height and the flow Reynolds number (defined below), the flow will separate in the lee of the bump, with a distinct region of recirculating flow (Smith 1976). Our model will consider the case when the bump is represented by a slip surface, aimed at providing a control mechanism for flow separation, depicted schematically in figure 1(a).

On non-dimensionalising lengths by the channel half-width h^* , velocities by the maximum velocity U_m^* , and pressure by $\rho^*U_m^{*2}$, where ρ^* is the fluid density, the incompressible Navier–Stokes equations in Cartesian coordinates (x, y) can be written as

$$\frac{\partial u}{\partial t} + (u \cdot \nabla) u = -\nabla p + \frac{1}{Re} \nabla^2 u, \qquad (2.1a)$$

$$\nabla \cdot \boldsymbol{u} = 0, \tag{2.1b}$$

for the non-dimensional velocity $\mathbf{u} = (u, v)$ and pressure p; here the Reynolds number is defined as

$$Re = \frac{U_m^* h^*}{\nu^*}. (2.2)$$

Following the non-dimensionalisation, the wall-normal y-direction is defined on the interval $y \in [0, 2]$. The lower wall, y = 0, is split into three regions Γ_1 , Γ_2 and Γ_3 , with a

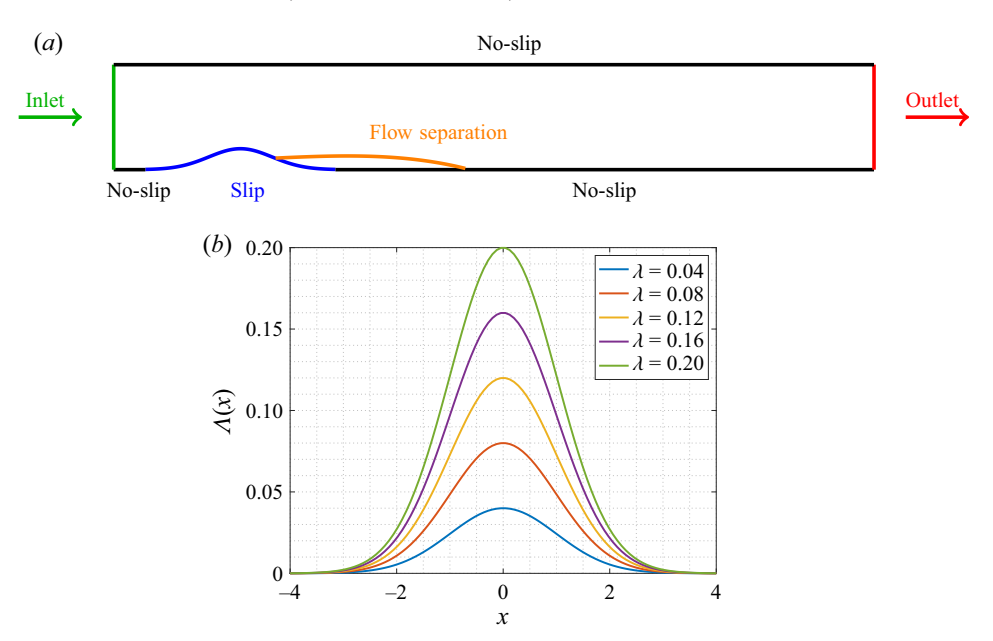


Figure 1. (a) Diagram of channel flow with slip applied to a Gaussian-shaped bump. Not drawn to scale. (b) Plot of the slip function $\Lambda(x)$, given by (2.5), for effective slip lengths $\lambda = 0.04, 0.08, 0.012, 0.16, 0.2$.

Gaussian-shaped bump imposed along the middle region Γ_2 , centred at x = 0. Turning to the question of the flow boundary conditions, we apply the no-slip condition

$$u = v = 0, (2.3)$$

to the upper wall and along the regions Γ_1 and Γ_3 of the lower wall. In the bump region, Γ_2 , a linear Robin-type slip condition is coupled with the no penetration condition as

$$u - \Lambda(x) \frac{\partial u}{\partial n} = 0$$
 and $v = 0$, (2.4*a*,*b*)

where *n* denotes the direction normal to the lower wall. We set

$$\Lambda(x) = \lambda e^{-x^2/2},\tag{2.5}$$

to model slip along the length of the bump for an effective slip length λ . This choice for the wall slip was chosen to avoid abrupt changes in the boundary conditions near the ends of the bump region, Γ_2 . Thus, slip decreases smoothly to no-slip beyond the bump. A plot of the slip function $\Lambda(x)$ is shown in figure 1(b) for an effective slip length λ increased from 0.04 to 0.2 monotonically in intervals of $\Delta\lambda = 0.04$.

At the channel inlet, the velocity u is assumed to be fully developed plane-Poiseuille flow

$$\mathbf{u} = (u(y), 0) = (2y - y^2, 0),$$
 (2.6)

while at the channel outlet we impose the outflow boundary condition

$$\nabla u \cdot n = 0 \quad \text{and} \quad p = 0, \tag{2.7a,b}$$

where n is the unit normal vector.

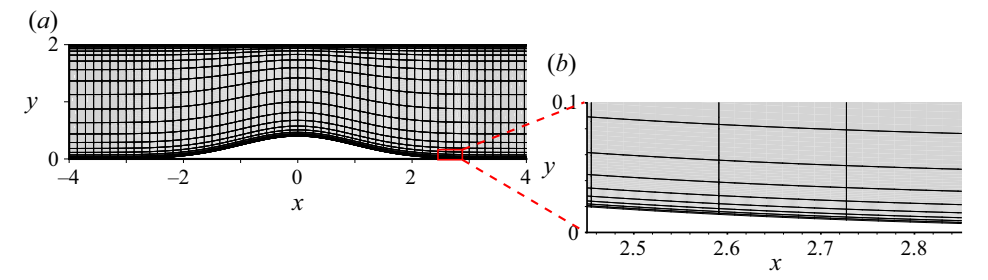


Figure 2. Diagram of the mesh in the region of the Gaussian-shaped bump. Mesh distributed uniformly and non-uniformly along the respective *x*- and *y*-directions.

2.2. Numerical method

Direct numerical simulations of the channel flow were performed using Nektar++, an open-source spectral/hp element method that exploits the solver IncNavierStokesSolver (Cantwell *et al.* 2015). The Gaussian-shaped bump was imposed in region Γ_2 of the lower wall using a coordinate transformation

$$x = \bar{x}, y = f(\bar{x}, \bar{y}),$$
(2.8a)

where the function $f = f(\bar{x}, \bar{y})$ maps the computational coordinates onto the physical Cartesian coordinates (Serson, Meneghini & Sherwin 2016). The mapping function

$$f(\bar{x}, \bar{y}) = \bar{y} + \frac{Ae^{-\bar{x}^2/2}}{2\sqrt{2\pi}} \frac{\tanh(2 - \bar{y})}{\tanh(2)},$$
 (2.8b)

establishes a Gaussian-shaped bump, of amplitude A, centred about x=0. The \bar{y} -dependent hyperbolic tangent function was included in the mapping to establish an appropriate transformation of the mesh in the (x,y)-plane, as depicted in figure 2. Additionally, the aspect ratio $\eta=1/A$ is introduced to characterise the non-dimensional channel half-width h=1 with respect to the bump amplitude A.

In addition to simplifying the solution of the governing equations, the mapping transformation (2.8) simplifies the implementation of the slip condition (2.4); applying the Robin-type slip condition to the computational coordinates (\bar{x}, \bar{y}) removes the need for computing wall-normal gradients along a curved surface. Consequently, the non-dimensional Navier–Stokes equations (2.1) are modified accordingly, so that Nektar++ numerically computes the base flow in the computational domain (\bar{x}, \bar{y}) , with post-processing then required to present results in the physical Cartesian coordinate geometry (x, y). Moreover, it was necessary to transform solutions into their Cartesian representation with velocities u^i computed via the repeated index summation convention, as

$$u^{i} = \frac{\partial x^{i}}{\partial \bar{x}^{j}} \bar{u}^{j}, \tag{2.9}$$

where \bar{u}^i denotes the transformed velocity field (Serson 2017).

The computational domain Ω was decomposed as $\Omega_{\bar{x}} \times \Omega_{\bar{y}} = [-4, 20] \times [0, 2]$, with the lower wall given by the streamwise intervals $\Gamma_1 = [-4, -3]$, $\Gamma_2 = [-3, 3]$ and $\Gamma_3 = [3, 20]$. A suitable mesh was generated using Gmsh (Geuzaine & Remacle 2009), consisting of 4611 quadrilateral elements, and nodes $N_{\bar{x}} = 160$ and $N_{\bar{y}} = 30$ along the

respective computational streamwise \bar{x} - and wall-normal \bar{y} -directions. Moreover, the mesh was uniformly and non-uniformly distributed along the \bar{x} - and \bar{y} -directions, respectively. The latter distribution was implemented to fully resolve the flow dynamics near the channel walls and in the bump region. The grid spacing along the streamwise \bar{x} -direction was fixed throughout the computational domain and was given in wall units as $\Delta \bar{x} = 0.15$. Due to the non-uniform distribution of points along the wall-normal \bar{y} -direction, a maximum grid spacing of $\Delta \bar{y}_{max} = 0.25$ was implemented at the channel centre, while a minimum grid spacing of $\Delta \bar{y}_{min} \approx 0.01$ was utilised near the channel walls. A depiction of the mesh, in the physical Cartesian coordinate system (x, y), is shown in figure 2.

The corresponding wall-normal grid spacing in non-dimensional wall distance y+ units is given by

$$y^{+} = \frac{\Delta y^{*} u_{\tau_{w}}^{*}}{v^{*}}, \tag{2.10a}$$

where the dimensional friction velocity and wall shear stress are defined as

$$u_{\tau_w}^* = \sqrt{\frac{\tau_w^*}{\rho^*}} \quad \text{and} \quad \tau_w^* = \mu^* \left. \frac{\partial u^*}{\partial y^*} \right|_{y^*=0},$$
 (2.10*b,c*)

and μ^* is the dynamic viscosity. Using the length and velocity scales, h^* and U_m^* , the wall distance is recast as

$$y^{+} = \Delta \bar{y} \sqrt{Re \left. \frac{\partial u}{\partial y} \right|_{y=0}}, \tag{2.11}$$

with $\partial u/\partial y$ as given at the channel inlet. Thus, $y^+ \approx 0.4$ and $y^+ \approx 0.6$ for the Reynolds numbers Re = 2000 and Re = 4000, respectively. A similar expression applies for the streamwise grid spacing x^+ , with $x^+ = 8$ and $x^+ = 10$ for the two Reynolds numbers modelled.

In the work described here, DNS was undertaken for a Gaussian-shaped bump with a fixed aspect ratio $\eta = 0.5$, that is, A = 2 in (2.8). The amplitude A of the bump was chosen to be large enough to form a well-defined separation bubble on the rear side of the bump. Setting A=2 was found to establish a significant region of separation in the instance that no-slip was applied to the lower surface, and best demonstrates the control benefits brought about by the application of slip. The slip parameter λ was then varied from 0 (corresponding to no-slip) through to 0.2 at step intervals $\Delta \lambda = 0.02$, for Reynolds numbers Re = 2000 and Re = 4000. (Our choices of Reynolds numbers Rewere chosen to be below the classical critical Reynolds number for channel flow, thus serving to control the development of any potential linear disturbances introduced due to, for example, the numerical discretisation.) For all simulations presented, eighth-order Lagrange polynomials were used to approximate the solution, while time integration was performed using a third-order implicit–explicit scheme with a time step $\Delta t = 10^{-3}$. A thorough convergence study was undertaken, which included varying the polynomial order of the Lagrange polynomials, mesh size, channel length and time step Δt . Parameter settings were carefully chosen to ensure all results were grid independent (to within graphical accuracy).

Channel flow over the bump was then simulated, from a stationary initial condition, until a steady state was realised. Table 1 presents the minimum value of the streamwise u-velocity, $\min(u)$, found in the separation bubble that forms on the rear side of the bump, in the instance the Reynolds number Re = 4000 and slip length $\lambda = 0$. Results are presented at non-dimensional time t = 200, for four mesh configurations. Test C00

Test	$\Omega_{ar{x}}$	$N_{\bar{x}}$	$N_{ar{y}}$	min(u)
C00	[-4, 20]	160	30	-0.091529
C01	[-4, 20]	320	30	-0.092264
C02	[-4, 20]	160	60	-0.094327
C03	[-4, 30]	160	30	-0.092179

Table 1. Minimum value of the streamwise u-velocity, $\min(u)$, obtained for Re = 4000, $\lambda = 0$ (no-slip), at time t = 200, and three mesh configurations. Test C00 are the settings used throughout this investigation; in test C01 the x-resolution is doubled; in test C02 the y-resolution is doubled; in test C03 a larger streamwise computational domain is modelled.

corresponds to those mesh settings described above, and which were used throughout the subsequent investigation. In tests C01 and C02, the mesh resolution was doubled along the x- and y-directions, respectively, while a larger streamwise computational domain was modelled in test C03. Doubling the mesh resolution along the x- and y-directions and increasing the channel length were found to bring about very small differences in $\min(u)$, with computations identical to at least two decimal places.

3. Results

To provide a reference point from which to explore the effect of slip on flow separation, we first present results for the no-slip channel. Figure 3 depicts the evolution of the streamwise u-velocity in the channel as the flow develops downstream (from left to right) over the Gaussian-shaped bump. The Reynolds number Re = 2000 and slip length $\lambda = 0$, that is, no-slip (2.3) was applied across the full length of the lower wall. Solutions are plotted at four successive times, t = 20, t = 40, t = 60 and t = 100, with yellow contours (near the channel centre) matched to u = 1 and blue contours (near the channel walls) to $u \leq 0$. In order to highlight the recirculation region(s), we present a secondary plot that highlights the regions, in red, for which u < 0. (The yellow-blue colour scheme used to display contour levels in figure 3, and subsequent figures was restricted to the interval $u \in [0, 1]$ to best illustrate the development of the flow from one time instant to the next. Variations in flow behaviour would be less discernible if each solution was plotted on their respective full u-velocity range. Secondary plots are included to help distinguish the regions of flow separation.) It is convenient to introduce x_s and x_r to denote the streamwise locations for the onset of separation and reattachment of the flow, respectively. As the flow advances downstream, the flow separates along the rear side of the bump near the streamwise location $x_s \approx 0.6$ (as a consequence of a sufficiently large adverse pressure gradient, induced by the channel constriction). The region of separation extends downstream, with flow reattachment moving farther along the channel as time increases, before eventually settling near $x_r \approx 8$. In addition to the separation bubble behind the bump, unsteady pockets of recirculating flow are established along the upper and lower walls that propagate downstream. Eventually, these unsteady separation pockets pass beyond the computational domain of interest, and the flow (including the separation bubble on the rear side of the bump) achieves a steady state. For Re = 2000, this steady state was realised at non-dimensional time t = 100.

The time evolution of the streamwise u-velocity is plotted in figure 4 at three fixed Cartesian locations (x, y) = (2.5, 0.2), (x, y) = (2.5, 1) and (x, y) = (2.5, 1.8). The first of these three points is located within the separation bubble that forms on the rear side of the bump, with the second and third points located about the channel centre

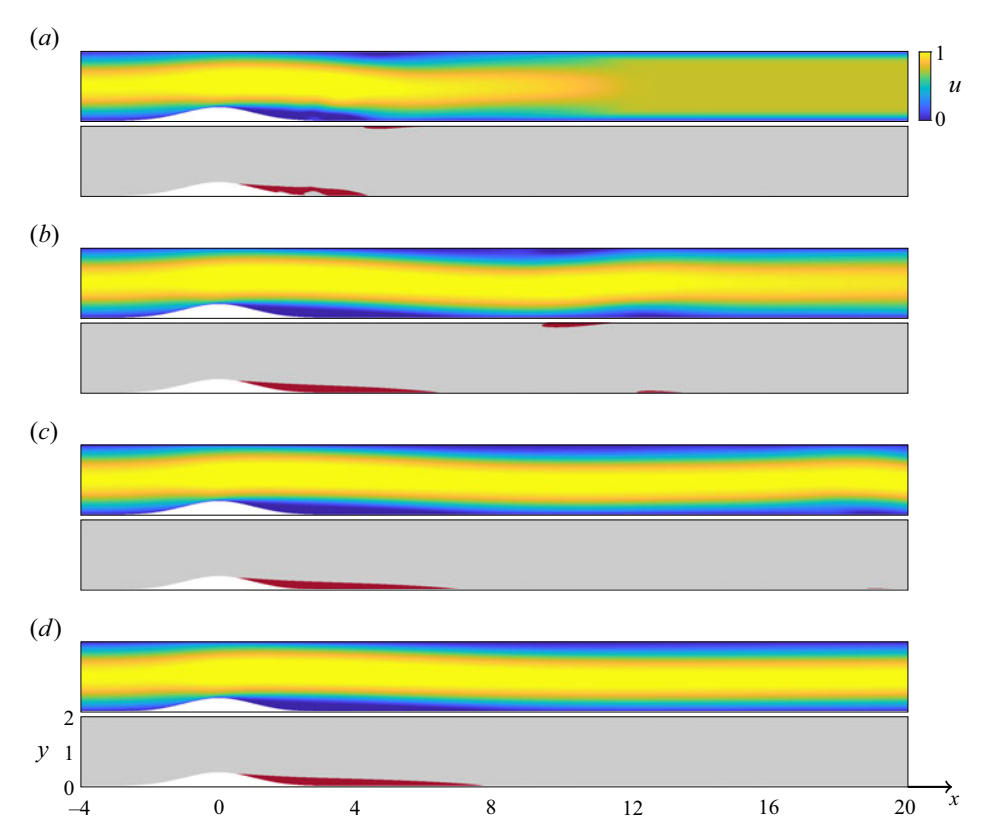


Figure 3. Contour plots illustrating the evolution of the streamwise u-velocity as the flow propagates downstream over the bump for a Reynolds number Re = 2000 and slip length $\lambda = 0$, i.e. no-slip. Solutions are plotted at times: (a) t = 20; (b) t = 40; (c) t = 60; (d) t = 100. At each time shown, the second plot highlights the regions of separation, in red, where u < 0.

and near the upper channel wall, respectively. Figure 4(a) illustrates the location of the three points relative to the bump and region of flow separation. The evolution of the flow, from a transient to steady state, can readily be seen in figures 4(b) and 4(c), for the Reynolds numbers Re = 2000 and Re = 4000, respectively. In each instance, there is a short transient period, in which the u-velocity field changes rapidly. However, after approximately t = 40, the streamwise u-velocity appears to have reached a steady state and is unchanged by further increments in time. As observed in the contour plots above, a constant negative valued u-velocity is realised at the point located within the separation bubble (blue solid line), while positive valued u-velocities are found at larger y-locations. Additionally, the u-velocity is marginally greater than unity at the channel centre (dashed red line), due to the formation of the separation bubble. Similar results are presented in figure 4(c) for the Reynolds number Re = 4000. Here we note that a steady state is not realised until non-dimensional time $t \approx 80$. Moreover, as a consequence of the flow developing downstream, longer time simulations were necessary (in both instances) to achieve a steady state at larger streamwise x-locations.

The above analysis was extended to include slip (2.4) along the bump region, Γ_2 . The main qualitative conclusion that can be drawn from our analysis is that slip can be used to delay the onset of separation and reduce the intensity of the separation bubble that forms along the rear side of the bump. This observation is demonstrated in figures 5

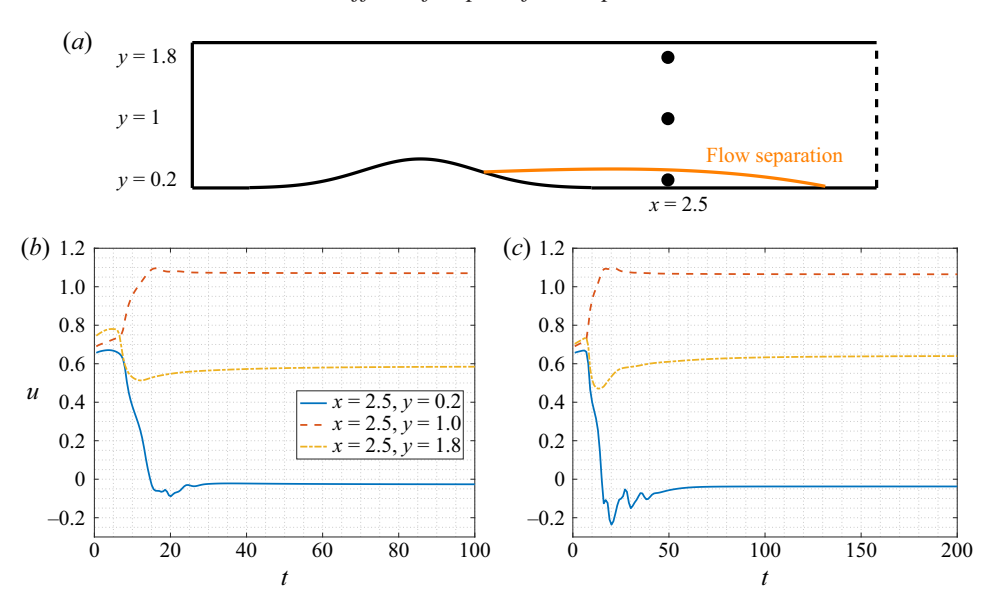


Figure 4. Time evolution of the *u*-velocity at three fixed locations, marked by solid dots as shown in (a) (x, y) = (2.5, 0.2) (solid lines), (x, y) = (2.5, 1) (dashed) and (x, y) = (2.5, 1.8) (chain), for a slip length $\lambda = 0$, and the Reynolds number (b) Re = 2000, (c) Re = 4000.

and 6, which display contours of the streamwise velocity for two representative Reynolds numbers, Re = 2000 and Re = 4000. In each instance, the slip length λ is increased from zero to 0.2 monotonically down the figure in intervals of $\Delta\lambda = 0.04$. All contour plots for Re = 2000 are plotted at non-dimensional time t = 100, which was again sufficient to achieve a steady state. For the larger Reynolds number, Re = 4000, it was necessary to extend DNS computations to larger time, with a steady state eventually realised at t = 200. Moreover, simulation results for the two Reynolds numbers are presented for the same slip lengths, to facilitate comparison of the effect of slip on flow separation. As in figure 3, yellow and blue contours are matched to the respective streamwise velocities u = 1 and $u \le 0$, while the secondary plots highlight the regions, in red, of recirculation (that is, where u < 0).

As the slip length λ increases, the onset of separation along the rear side of the bump is delayed, that is, the streamwise location x_s moves downstream. Additionally, the streamwise location x_r at which the flow reattaches is generally found to move upstream. (There are a few exceptions to this, for the Reynolds number Re = 4000 and small slip lengths λ . This particular flow characteristic will be discussed in greater detail below.) Thus, the length of the separation bubble, behind the bump, decreases as the slip length λ increases. Moreover, the 'thickness' of the separation bubble diminishes as λ increases. This behaviour is qualitatively equivalent for both Reynolds numbers Re under consideration, although for a fixed slip length λ , flow reattachment is always found at larger streamwise locations for Re = 4000, as one would anticipate on the basis of the analysis of Smith (1976) for the full no-slip case. Eventually, the streamwise locations for the onset of separation x_s and reattachment x_r coalesce and the flow no longer separates. For those parameters considered in figures 5 and 6, separation does not occur for a slip length $\lambda = 0.2$.

Velocity profiles of the streamwise *u*-velocity are plotted in figure 7 for three fixed streamwise *x*-positions: the bump centre (x = 0); the recirculating region (x = 4); and

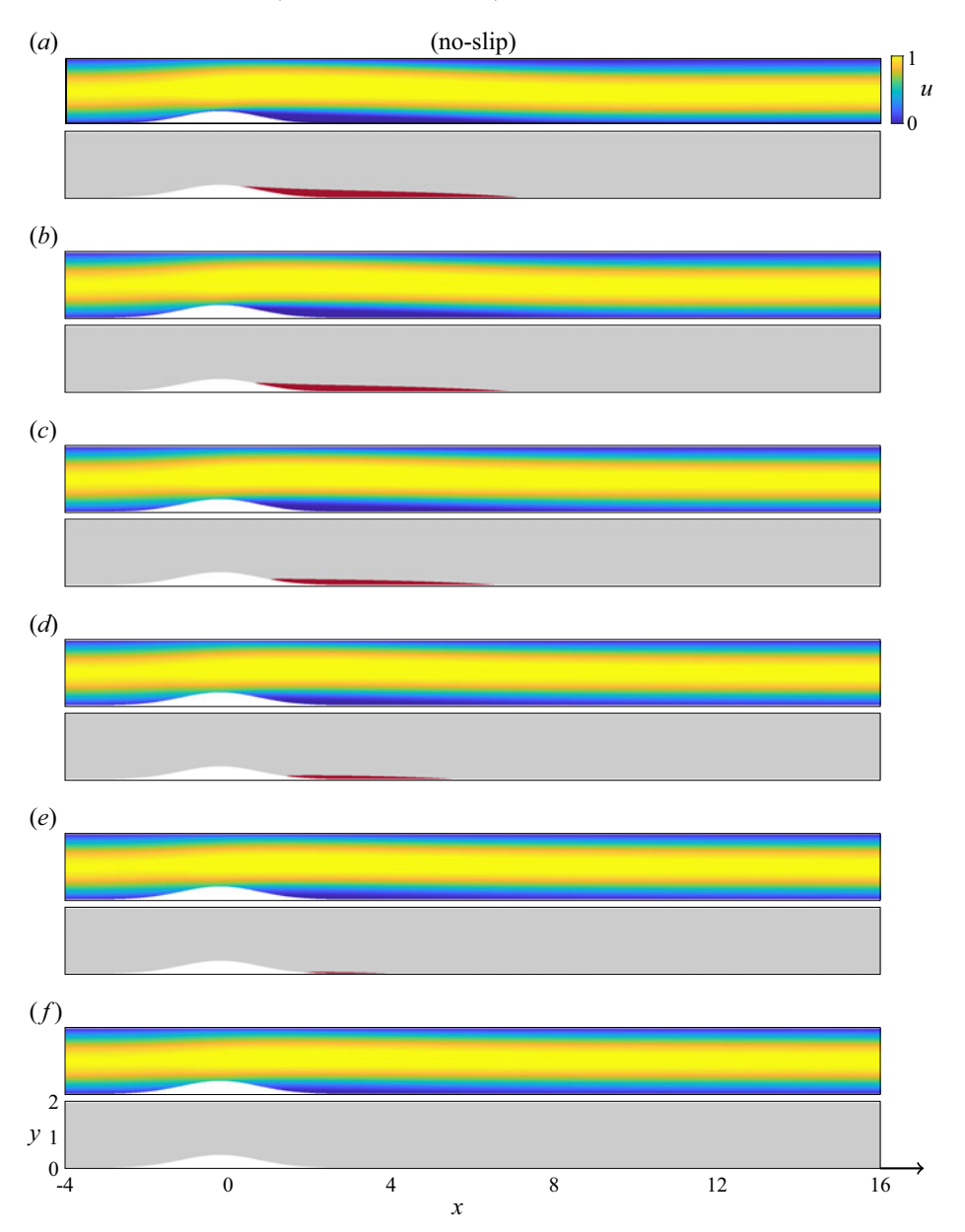


Figure 5. Contour plots of the streamwise *u*-velocity for the Reynolds number Re = 2000 and slip length (a) $\lambda = 0$, (b) $\lambda = 0.04$, (c) $\lambda = 0.08$, (d) $\lambda = 0.12$, (e) $\lambda = 0.16$ and (f) $\lambda = 0.2$. Secondary plots highlight the regions of separation, in red, where u < 0.

far downstream of the separation bubble (x = 19). Results are plotted for slip lengths $\lambda = 0$ (solid line), $\lambda = 0.08$ (dashed) and $\lambda = 0.16$ (chain), with plots on the upper row matched to the Reynolds number Re = 2000 and those on the lower row to Re = 4000. In addition, each solution has been scaled to have a maximum value of unity; the emergence of flow separation and the application of slip to the lower channel surface brings about a small increase in the u-velocity maximum. In figures 7(a) and 7(d) (that correspond to x = 0), the application of no-slip along the bump region can be seen to establish a

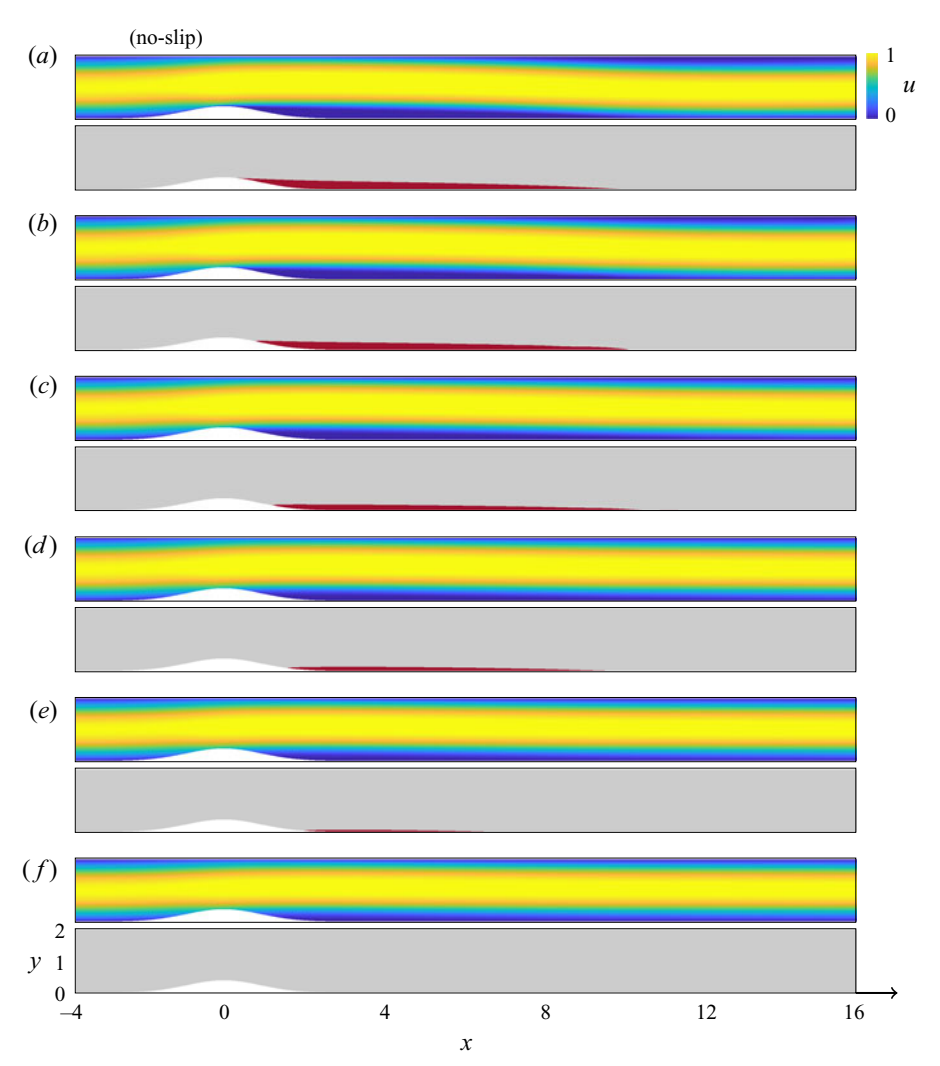


Figure 6. Same as figure 5, but for the Reynolds number Re = 4000 and non-dimensional time t = 200. (a) $\lambda = 0$, (b) $\lambda = 0.04$, (c) $\lambda = 0.08$, (d) $\lambda = 0.12$, (e) $\lambda = 0.16$ and (f) $\lambda = 0.2$.

sharp change in the *u*-velocity field near the lower channel wall (solid lines), while slip induces a non-zero velocity at the bump tip (dashed and chain lines). Moreover, the bump has shifted the maximum *u*-velocity downwards towards the lower channel wall. At the streamwise position x = 4, plotted in figures 7(b) and 7(e), the *u*-velocity at the lower wall is zero in each instance; this particular location is found in region Γ_3 that is downstream of the slip region Γ_2 . From figures 7(b) and 7(e) the thickness of the separation bubble that forms on the rear side of the bump can be estimated. For the case without slip, the *u*-velocity is negative for $y \le 0.2$ and $y \le 0.3$, for the respective Reynolds numbers Re = 2000 and Re = 4000. Hence, the region of separation thickens as the Reynolds number increases. Furthermore, the application of slip to the bump region reduces the thickness of the separation bubble. At the downstream location, x = 19, the flow recovers behaviour consistent with the typical parabolic profile of fully developed plane-Poiseuille flow, as can be seen in figures 7(c) and 7(f). We note that there remains

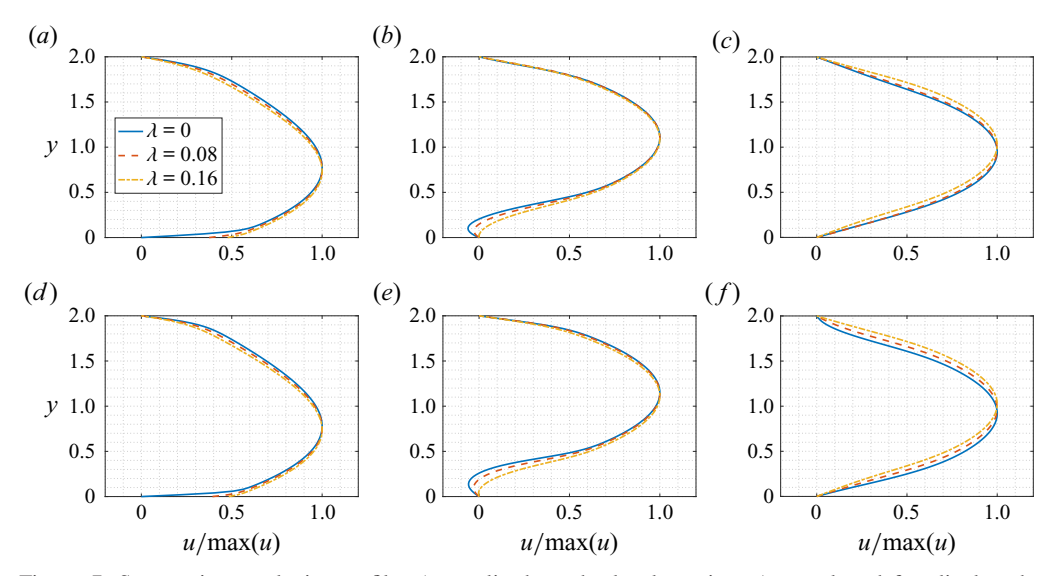


Figure 7. Streamwise *u*-velocity profiles (normalised on the local maximum) are plotted for slip lengths $\lambda = 0$ (solid lines), $\lambda = 0.08$ (dashed) and $\lambda = 0.16$ (chain), for the Reynolds number (a–c) Re = 2000 and (d–f) Re = 4000, at the streamwise locations x = 0, x = 4 and x = 19, respectively. Results are plotted at non-dimensional time t = 100 and t = 200 for Re = 2000 and Re = 4000, respectively.

a small downwards shift in the maximum velocity, especially in the case of no-slip. This is a direct consequence of the flow requiring a greater streamwise domain to adjust to the pocket of separated flow. Eventually, for large enough x, the flow will evolve to fully developed plane-Poiseuille flow.

The effects of the slip length λ and Reynolds number Re on the size of the separation bubble that forms along the rear side of the bump, are further illustrated in figure 8. Streamlines of the steady flow are plotted for slip lengths $\lambda=0$ (no-slip), $\lambda=0.06$, $\lambda=0.12$ and $\lambda=0.18$. Within each subplot, solutions are displayed for both Reynolds numbers, Re=2000 and Re=4000. As noted above, the recirculation region is longer and thicker for the larger Reynolds number. Additionally, the significant influence of slip is evident in both cases, establishing both a delay in the onset of separation and a shortening of the bubble's length. However, for Re=4000, a larger slip length λ is always necessary to reduce the streamwise length of the recirculation region; separation is suppressed by setting $\lambda=0.18$ in the instance Re=2000, while a small region of recirculation is found in the streamwise interval 2 < x < 4 for Re=4000. However, as shown in figure 6(f), this disappears for $\lambda=0.2$.

The non-dimensional shear stress at the wall

$$\tau_w = \left. \frac{\partial u}{\partial y} \right|_{y=0},\tag{3.1}$$

is plotted in figure 9 for slip lengths $\lambda = 0$ (solid lines), $\lambda = 0.1$ (dashed) and $\lambda = 0.2$ (chain). Results in figure 9(a) are for a Reynolds number Re = 2000, while those in figure 9(b) correspond to Re = 4000. For both Reynolds numbers under consideration, the wall shear stress τ_w increases along the front side of the bump, before decreasing sharply along the rear side. This behaviour is more pronounced for the larger Reynolds number. When the slip length $\lambda = 0$ (the classical no-slip case), a negative valued τ_w is realised that extends a significant streamwise length downstream until flow reattachment

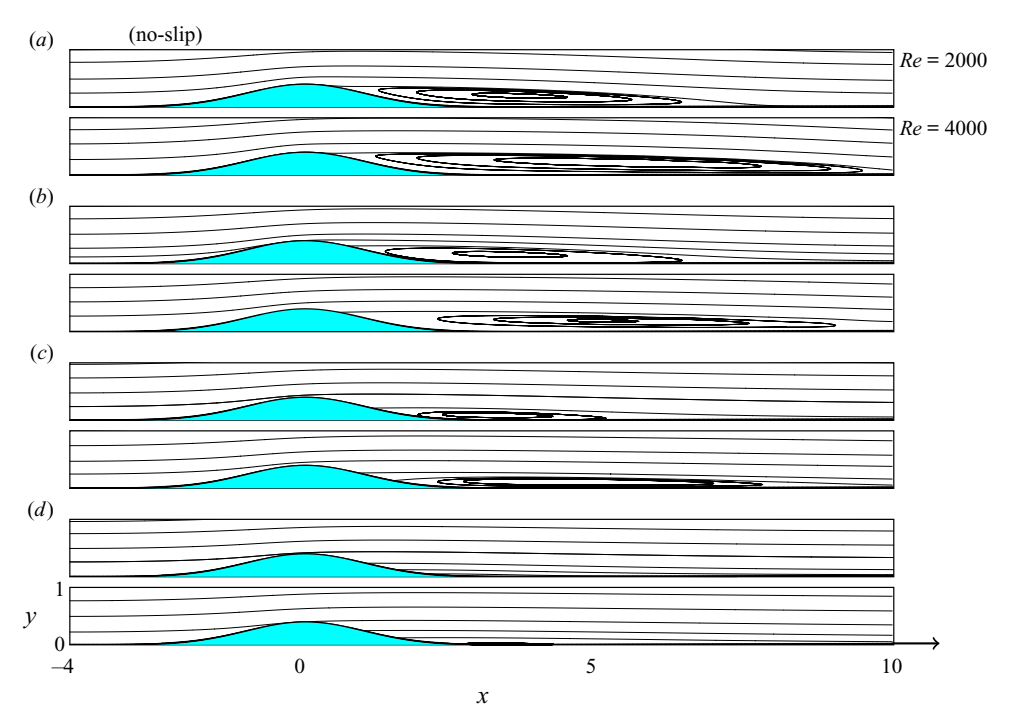


Figure 8. Streamlines of the steady flow in the region of the bump, obtained at non-dimensional time t=100 and t=200 for the respective Reynolds numbers Re=2000 and Re=4000. The slip length (a) $\lambda=0$, (b) $\lambda=0.06$, (c) $\lambda=0.12$ and (d) $\lambda=0.18$.

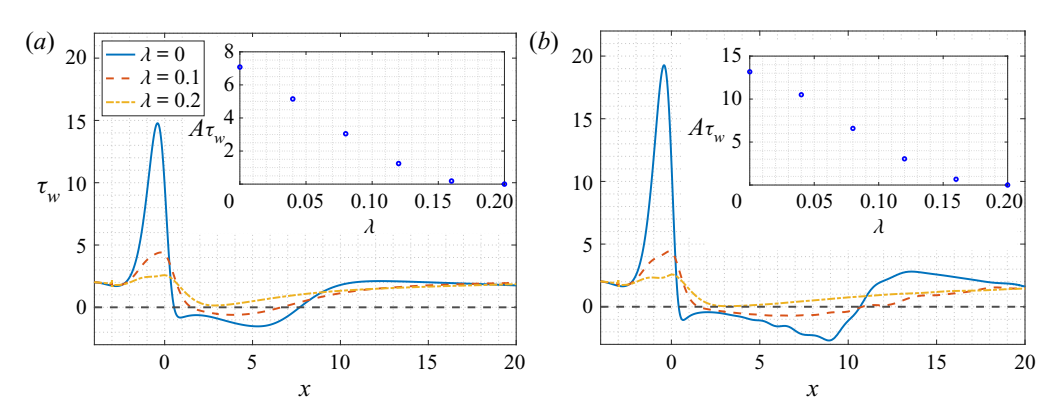


Figure 9. Wall shear stress, τ_w , for the Reynolds numbers (a) Re = 2000 at t = 100, (b) Re = 4000 at t = 200. The slip length $\lambda = 0$ (solid lines), $\lambda = 0.1$ (dashed) and $\lambda = 0.2$ (chain). The insert plots depict the area of the separated region A_{τ_w} , as given by (3.2), as a function of the slip length λ .

occurs (which is consistent with that presented above in figures 5–8). Downstream of the reattachment location, the wall shear stress τ_w approaches a value of 2, which is consistent with that expected of the fully undisturbed plane-Poiseuille flow in this region (2.6). The application of slip to the bump surface significantly reduces both the increase and decrease in the wall shear stress τ_w along the respective front and rear sides of the bump. Indeed, when the slip length $\lambda = 0.2$, $\tau_w > 0$ for all streamwise *x*-positions.

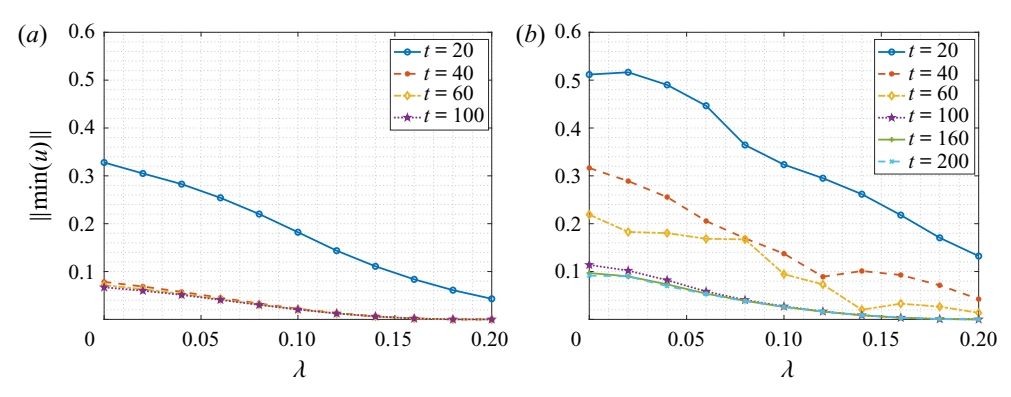


Figure 10. Plots of the absolute value of the minimum of the streamwise *u*-velocity, $\|\min(u)\|$, found within the separation bubble on the rear side of the bump, as a function of the slip length λ . (a) Re = 2000 and (b) Re = 4000.

The insert plots in figure 9(a) and 9 (b) illustrate how the area of the separated region

$$A_{\tau_w} = \left| \int_{x_s}^{x_r} \tau_w(x) \, \mathrm{d}x \right|,\tag{3.2}$$

varies in relation to the slip length λ , for the Reynolds numbers Re = 2000 and Re = 4000. For the no-slip case ($\lambda = 0$), the area of the separated region $A_{\tau_w} \approx 7$ when Re = 2000, whereas for Re = 4000 the area $A_{\tau_w} \approx 13$. The area of the separated region A_{τ_w} is approximately halved when the slip length $\lambda = 0.08$, while A_{τ_w} is equal to zero in both cases (i.e. no separated flow), for $\lambda = 0.2$.

The intensity of the recirculation region, on the rear side of the bump, can be quantified by computing the absolute value of the minimum of the streamwise u-velocity, $\|\min(u)\|$. In figure 10, $\|\min(u)\|$ is plotted as a function of the slip length λ , for both Reynolds numbers Re=2000 and Re=4000. In addition, results are shown at several points in time, providing a further demonstration of the flow evolution, and confirmation that a steady state is achieved for sufficiently large time. Convergence to a steady state is realised by non-dimensional time t=60 for Re=2000 and t=160 for Re=4000, respectively. Additionally, for suitably large time, $\|\min(u)\|$ is found to decrease linearly with the slip length λ , with no separation bubble forming behind the bump for $\lambda \geqslant 0.18$ and $\lambda \geqslant 0.2$ for the respective Reynolds numbers Re=2000 and Re=4000. Furthermore, the intensity of the separation bubble is greater for the larger Reynolds number, especially during the initial stages of the numerical simulation.

In figure 11(a) we present plots of the position of the onset of separation, which can readily be seen to shift along the right-hand side of the bump as slip increases. The onset occurs earlier in space for $\lambda = 0$ and 0.04 when Re = 4000, almost at the same position for both Reynolds numbers for $\lambda = 0.08$ and 0.12, and slightly earlier for $\lambda = 0.16$ at Re = 4000.

To quantify the length of the separation bubble, we define \mathcal{L}_x as the length of the separation bubble measured along the *x*-axis, such that $\mathcal{L}_x = x_r - x_s$. In figure 11(*b*), the variation of \mathcal{L}_x with the slip length λ is shown. The length of the separation bubble is larger for the higher Reynolds number and, in both cases, \mathcal{L}_x decreases to zero as slip increases, with critical values of $\lambda = 0.18$ for Re = 2000 and $\lambda = 0.2$ for Re = 4000. Interestingly, we also note from figure 11 that for the higher Reynolds number case, slip does not have a monotonic effect upon the length of the separation bubble, only showing clear signs of

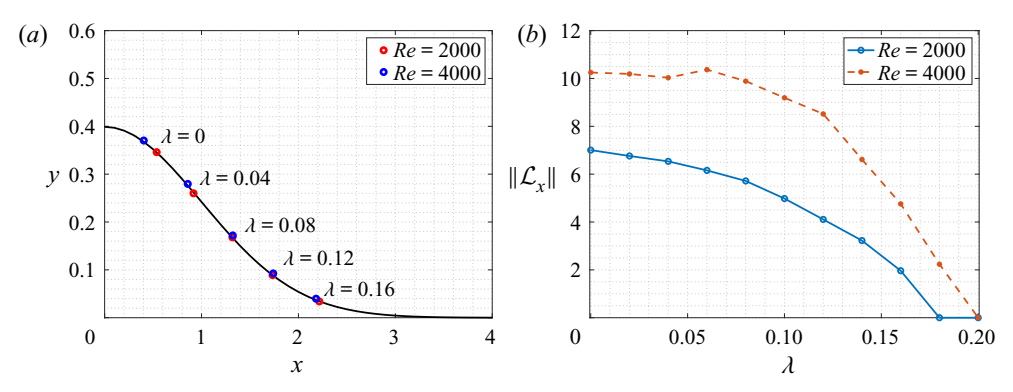


Figure 11. Plots of (a) the position x_s for the onset of separation and (b) the absolute value of the bubble length \mathcal{L}_x versus the slip length λ . Results are shown at t = 100 for Re = 2000 and t = 200 for Re = 4000.

a decrease when λ is above 0.06. We conjecture that this particular feature may be due to the fact that, for a higher Reynolds number where the intensity of separation is enhanced, a moderate slip length (that is, $\lambda < 0.06$) is not sufficient to counteract the reversed flow. Thus, only for $\lambda > 0.06$ does the beneficial effect of slip become evident.

3.1. Skin-friction and pressure drag coefficients

Skin-friction and pressure at the wall are defined locally by the non-dimensional coefficients

$$c_f(x) = \frac{2\tau_w^*(x)}{\rho^* U_w^{*2}}$$
 and $c_p(x) = \frac{2p^*(x)}{\rho^* U_w^{*2}}$, (3.3*a*,*b*)

(Banchetti, Luchini & Quadrio 2020). Using the length h^* , velocity U_m^* and pressure $\rho^* U_m^{2*}$ scales, the skin-friction and pressure coefficients are recast as

$$c_f(x) = \frac{2}{Re} \tau_w(x)$$
 and $c_p(x) = 2p(x)$, (3.4*a*,*b*)

where $\tau_w(x)$ denotes the non-dimensional shear stress at the wall given by (3.1). Effectively, the skin-friction coefficient $c_f(x)$ is the wall-shear stress $\tau_w(x)$ plotted in figure 9, scaled by the factor 2/Re.

In order to demonstrate the effect of slip on the pressure field over the bump, the pressure distribution p is plotted in figure 12, for the Reynolds number Re = 2000 and slip lengths $\lambda = 0$, $\lambda = 0.08$ and $\lambda = 0.16$. Pressure decreases as the flow passes from left to right over the bump, with a local minimum found shortly after the bump tip due to the negative wall curvature. For those slip cases shown, the local maximum found on the leeward side of the bump decreases, while the local minimum located about the bump tip shows clear signs of a reduced intensity; lighter blue contours.

The skin-friction and pressure contributions to the total drag are defined by Mollicone *et al.* (2017) as

$$C_f = \frac{1}{L_x} \int_{\Omega_{\bar{x}}} c_f(x) \, \mathrm{d}x \quad \text{and} \quad C_p = -\frac{1}{L_x} \int_{\Omega_{\bar{x}}} c_p(x) \boldsymbol{i} \cdot \boldsymbol{n} \, \mathrm{d}x, \tag{3.5a,b}$$

where L_x denotes the streamwise length of the computational domain $\Omega_{\bar{x}}$, i represents the unit vector in the streamwise x-direction and n again denotes the unit normal vector that

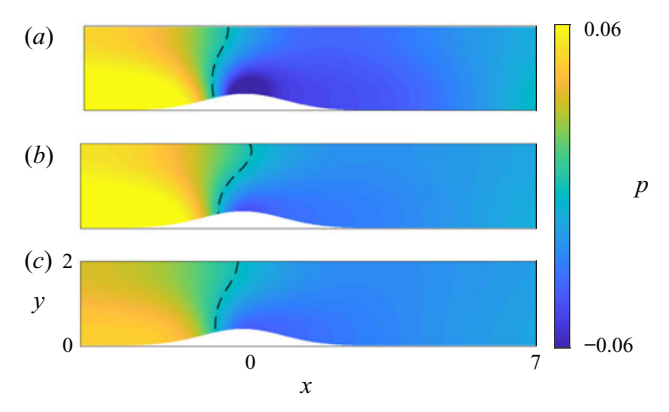


Figure 12. Contour plots of the pressure p in the (x, y)-plane, for the Reynolds number Re = 2000, and slip lengths $(a) \lambda = 0$, $(b) \lambda = 0.08$ and $(c) \lambda = 0.16$. Thick dashed black lines indicate p = 0.

points into the fluid domain. In (3.5b), the scalar product $i \cdot n \neq 0$ along the bump surface and zero elsewhere. Thus, the contribution of the pressure drag C_p to the total drag comes only from the pressure acting on the bump wall.

The respective percentage reductions in the skin-friction drag C_f and pressure drag C_p are computed using the formulae

$$\mathcal{R}_{C_f}(\%) = 100 \left(1 - \frac{C_{f,\lambda}}{C_{f,0}} \right) \quad \text{and} \quad \mathcal{R}_{C_p}(\%) = 100 \left(1 - \frac{C_{p,\lambda}}{C_{p,0}} \right),$$
 (3.6a,b)

where $C_{f,\lambda}$ and $C_{p,\lambda}$ represent the respective skin-friction and pressure components of drag in the instance slip (with slip length λ) is applied to the bump surface. Skin-friction and pressure drag components, $C_{f,0}$ and $C_{p,0}$, then denote the reference case in which no-slip (that is, $\lambda = 0$) is applied along the channel walls.

Total drag is defined as the sum of the skin-friction drag and pressure drag:

$$\mathcal{D}_{\lambda} = C_{f,\lambda} + C_{p,\lambda}. \tag{3.7}$$

Therefore, the total percentage drag reduction is obtained via the formula

$$\mathcal{R}_{\mathcal{D}}(\%) = 100 \left(1 - \frac{\mathcal{D}_{\lambda}}{\mathcal{D}_0} \right), \tag{3.8}$$

where $\mathcal{D}_0 = C_{f,0} + C_{p,0}$.

The total percentage drag reduction is plotted in figure 13 as a function of the slip length λ (yellow squares), together with the corresponding percentage reductions in the skin-friction drag (blue circles) and pressure drag (red diamonds), for the Reynolds numbers Re = 2000 and Re = 4000. A peak percentage reduction in the skin-friction drag is achieved in both instances for a slip length $\lambda \approx 0.08$, while the percentage reduction in the pressure drag increases almost linearly with λ . Overall, the total percentage drag reduction increases with an increasing slip length λ , with 27% and 35% total drag reductions achieved in the instance the slip length $\lambda = 0.2$, for Re = 2000 and Re = 4000, respectively.

3.2. Effect of slip applied across the entire lower wall

The question of why we have chosen to apply slip along a specific streamwise region rather than across the full length of the lower surface is an obvious one. From the perspective of

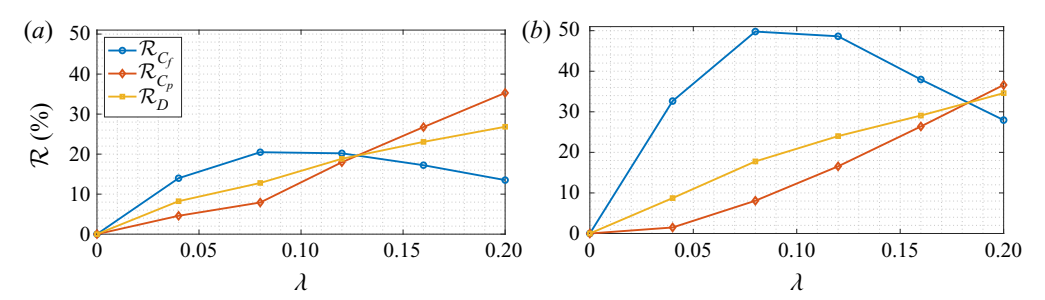


Figure 13. Skin-friction (blue circles), pressure (red diamonds) and total (yellow squares) percentage drag reduction as a function of the slip length λ , for the Reynolds numbers (a) Re = 2000 and (b) Re = 4000.

industrial applications, such as surface coatings, the implications of covering an entire surface versus a targeted area can have a substantial impact on economic costs. Therefore, if it is possible to achieve the same laminar flow control benefits at a reduced expense, it is generally advisable to do so. In the following, we compare the benefits of applying slip across the entire lower wall, Γ , with that realised when slip is limited to the bump region, Γ_2 .

Slip is applied across the full length of the lower wall, Γ , by recasting the coupled linear Robin-type slip boundary condition and no-penetration condition (2.4) as

$$u - \lambda \frac{\partial u}{\partial n} = 0$$
 and $v = 0$, (3.9*a*,*b*)

where the slip length λ is constant and n again denotes the direction normal to the lower wall. As before, all results are independent of the mesh used.

A quantitative analysis of the two approaches to slip application is reported in table 2. Here the minimum value of the streamwise u-velocity within the separation bubble, $\min(u)$, is tabulated, for Reynolds numbers Re = 2000 and 4000, at the respective times t = 100 and t = 200, that is, those points in time that a steady state has been realised. (Subscripts Γ and Γ_2 represent the application of slip to the full lower surface and to the bump region.) Moreover, calculations are presented for four slip lengths $\lambda \in [0.05, 0.2]$. In general, $\min(u)$ is reduced when slip is applied across the entire lower wall, that is, the intensity of the separation bubble decreases. Additionally, flow separation is inhibited (that is, $\min(u) = 0$) at smaller values of the slip length λ when slip is applied across the full length of the lower surface; $\lambda = 0.15$ is sufficient to stop the flow separating for both Reynolds numbers under consideration, while marginally larger slip lengths are necessary to suppress flow separation when slip is limited to the bump region.

In conclusion, applying slip across the full length of the lower wall inhibits the emergence of flow separation at smaller slip lengths λ , but the qualitative effect of slip on the flow separation dynamics is equivalent for both methods.

4. Concluding remarks

In this work, DNS have been performed to study the influence of a Robin-type slip boundary condition on the dynamics of the two-dimensional wake occurring behind a Gaussian-shaped bump in a channel. Specifically, it has been shown that surface slip: (i) decreases the intensity of the separation, (ii) delays, and ultimately inhibits, the onset of recirculation and in doing so (iii) reduces the dimensions of the separation bubble. There are a number of ways in which this work could be extended. One could vary the aspect

Re	λ	$\min(u)_{\Gamma_2}$	$\min(u)_{\Gamma}$
2000	0.05	-0.046031	-0.048523
2000	0.1	-0.020588	-0.011663
2000	0.15	-0.003980	0
2000	0.2	0	0
4000	0.05	-0.061278	-0.070396
4000	0.1	-0.026210	-0.014825
4000	0.15	-0.006091	0
4000	0.2	0	0

Table 2. Minimum value of the streamwise *u*-velocity, $\min(u)$, obtained for Reynolds numbers Re = 2000 and 4000, at times t = 100 and 200, respectively. Subscripts Γ and Γ_2 represent the application of slip to the entire lower surface and to the bump region.

ratio η and conduct a systematic study to investigate the effect of the bump's height in relation to different Reynolds numbers and slip lengths. (A brief summary of the effect of slip on other bump configurations is presented in the Appendix.) Alternatively, one could vary the length of the slip region Γ_2 along the lower wall and study the dynamics of the flow as a function of the dimensions of the slip region. Another direction would be to modify the type of application of slip on the bump. Slip is now applied in a Gaussian fashion to allow a smooth transition between the slip and no-slip region. This approach could be modified to determine a, possibly more efficient, way of introducing slip on a curved surface. Furthermore, one could extend the problem in three-dimensions, either in full three-dimensional (3-D) or quasi-3-D using a Fourier expansion in the span direction (Karniadakis 1990), and investigate the effect of slip applied both in the streamwise and spanwise directions on a fully 3-D bump.

Declaration of interests. The authors report no conflict of interest.

Author ORCIDs.

- Silvia Ceccacci https://orcid.org/0000-0002-8780-9739;
- Sophie A.W. Calabretto https://orcid.org/0000-0003-4582-2043;
- © Christian Thomas https://orcid.org/0000-0003-4324-530X;
- Dames P. Denier https://orcid.org/0000-0002-5428-2387.

Appendix. Effect of slip on different bump configurations

The above analysis was performed on the two-dimensional flow that develops in a channel over a bump of fixed aspect ratio $\eta=0.5$ (that is, an amplitude $A=1/\eta=2$), for the Reynolds numbers Re=2000 and Re=4000. This bump configuration and flow conditions were chosen as they were sufficient to establish a well-defined separation bubble on the rear side of the bump in the instance no-slip was applied to the channel walls. Hence, these particular parameter values were suitable for demonstrating the control benefits brought about by the application of slip to the bump surface. However, further bump configurations were modelled that illustrate comparable control of flow separation due to the application of slip. Table 3 presents the minimum value of the streamwise u-velocity, $\min(u)$, obtained for several bump-flow configurations characterised by the aspect ratio η , Reynolds number Re and slip length λ . The slip lengths labelled λ^* correspond to those parameters discussed at length in this paper, and were included here for reference.

Re = 2000			Re = 4000			Re = 5000		
λ	η	min(u)	λ	η	$\min(u)$	λ	η	min(u)
0*	0.5	-0.0670	0*	0.5	-0.0915	0	2	0
0.02*	0.5	-0.0599	0.02*	0.5	-0.0898	0	1	-0.0160
0.04*	0.5	-0.0512	0.04*	0.5	-0.0696	0.1	1	0
0.06*	0.5	-0.0409	0.06*	0.5	-0.0530	0	0.5	-0.1310
0.2*	0.5	0	0.08*	0.5	-0.0383	0.02	0.5	-0.1076
0.2	0.48	0	0.1*	0.5	-0.0303	0.04	0.5	-0.1007
0.2	0.47	0	0.2*	0.5	0	0.06	0.5	-0.0695

Table 3. Minimum value of the streamwise u-velocity, $\min(u)$, obtained for different bump-slip configurations characterised by the slip length λ , aspect ratio η and Reynolds number Re. Here * indicates those results presented in the main body of this paper.

Results presented in the first two columns of table 3 correspond to those Reynolds number modelled throughout this study (that is, Re = 2000 and Re = 4000). Two additional results are included in the first column that are matched to larger bumps, with the aspect ratio $\eta = 0.48$ and $\eta = 0.47$, respectively. In both instances, flow separation is inhibited by the application of slip with the slip length $\lambda = 0.2$ (i.e. the same as that found for $\eta = 0.5$).

The right-hand column of table 3 presents results corresponding to the Reynolds number Re = 5000. (Note that $y^+ \approx 0.7$ for Re = 5000.) When no-slip is applied to the same bump geometry modelled throughout this paper (i.e. $\eta = 0.5$), the minimum value of the streamwise u-velocity, $\min(u)$, is greater for Re = 5000 compared with those calculations obtained for the two smaller valued Reynolds numbers. Nevertheless, slip is again found to bring about favourable control benefits, with slip attenuating the intensity of the recirculation region and $\min(u)$ decreasing as the slip length λ increases. For smaller bump configurations, the flow does not separate under any circumstances (including no-slip) when the aspect ratio $\eta = 2$, whereas for $\eta = 1$ flow separation is inhibited for a small slip length $\lambda = 0.1$.

REFERENCES

BANCHETTI, J., LUCHINI, P. & QUADRIO, M. 2020 Turbulent drag reduction over curved walls. *J. Fluid Mech.* **896**, A10.

BERATLIS, N., BALARAS, E. & SQUIRES, K. 2018 The role of surface texturing on the physics of boundary layer separation over a bump. *Intl J. Heat Fluid Flow* 73, 223–235.

CANTWELL, C.D., et al. 2015 Nektar++: an open-source spectral/hp element framework. Comput. Phys. Commu. 192, 205–219.

CHANG, Z. & LU, Y. 2020 Fabrication of superhydrophobic surfaces with Cassie–Baxter state. J. Dispers. Sci. Technol. 45 (8), 1099–1111.

GEUZAINE, C. & REMACLE, J.-F. 2009 Gmsh: a 3-D finite element mesh generator with built-in pre- and post-processing facilities. *Intl J. Numer. Meth. Engng* **79** (11), 1309–1331.

HADJICONSTANTINOU, N.G. 2021 An atomistic model for the Navier slip condition. J. Fluid Mech. 912, A26.
HANKS, R.W. 1963 Laminar-turbulent transition for flow in pipes, concentric annuli, and parallel plates.
AIChE J. P9, 45–48.

KARNIADAKIS, G.E. 1990 Spectral element-Fourier methods for incompressible turbulent flows. *Comput. Meth. Appl. Mech. Engng* **80** (1), 367–380.

LAUGA, E. & COSSU, C. 2005 A note on the stability of slip channel flows. *Phys. Fluids* 17 (8), 088106.

LEGENDRE, D., LAUGA, E. & MAGNAUDET, J. 2009 Influence of slip on the dynamics of two-dimensional wakes. *J. Fluid Mech.* **633**, 437–447.

- MATTHEWS, M.T. & HILL, J.M. 2008 A note on the boundary layer equations with linear slip boundary condition. *Appl. Maths Lett.* 21 (8), 810–813.
- MIN, T. & KIM, J. 2004 Effects of hydrophobic surface on skin-friction drag. *Phys. Fluids* **16** (7), L55–L58. MOLLICONE, J.-P., BATTISTA, F., GUALTIERI, P. & CASCIOLA, C.M. 2017 Effect of geometry and Reynolds number on the turbulent separated flow behind a bulge in a channel. *J. Fluid Mech.* **823**, 100–133.
- NAVIER, C.L.M.H. 1823 Memoire sur les lois du mouvement des fluids. *Mem. Acad. Sci. Inst. Fr.* **6**, 389–416. SENGUPTA, A., SUMAN, V.K., SENGUPTA, T.K. & BHAUMIK, S. 2018 An enstrophy-based linear and nonlinear receptivity theory. *Phys. Fluids* **30** (5), 054106.
- SERSON, D. 2017 Numerical study of wings with wavy leading and trailing edges. PhD thesis, Imperial College, London.
- SERSON, D., MENEGHINI, J.R. & SHERWIN, S.J. 2016 Velocity-correction schemes for the incompressible Navier–Stokes equations in general coordinate systems. *J. Comput. Phys.* **316**, 243–254.
- SMITH, F.T. 1976 Flow through constricted or dilated pipes and channels: part 1. Q. J. Mech. Appl. Maths 29 (3), 343–364.
- SYCHEV, V.V., RUBAN, A.I., SYCHEV, V.V. & KOROLEV, G.L. 1998 Asymptotic Theory of Separated Flows. Cambridge University Press.
- THOMPSON, P.A. & TROIAN, S.M. 1997 A general boundary condition for liquid flow at solid surfaces. *Nature* 389, 360–362.
- VOROBYEV, A.Y. & GUO, C. 2015 Multifunctional surfaces produced by femtosecond laser pulses. *J. Appl. Phys.* 117 (3), 033103.
- WANG, C. & GHARIB, M. 2020 Effect of the dynamic slip boundary condition on the near-wall turbulent boundary layer. *J. Fluid Mech.* **901**, A11.
- WANG, G.J. & HADJICONSTANTINOU, N.G. 2019 Universal molecular-kinetic scaling relation for slip of a simple fluid at a solid boundary. *Phys. Rev. Fluids* 4, 064201.
- WHITE, A.H. & SMITH, F.T. 2012 Wall shape effects on multiphase flow in channels. *Theor. Comput. Fluid Dyn.* **26** (1), 339–360.
- Xu, H., Lombard, J.-E.W. & Sherwin, S.J. 2017 Influence of localised smooth steps on the instability of a boundary layer. *J. Fluid Mech.* **817**, 138–170.
- XU, H., SHERWIN, S.J., HALL, P. & WU, X. 2016 The behaviour of Tollmien–Schlichting waves undergoing small-scale localised distortions. *J. Fluid Mech.* **792**, 499–525.